Measurement of branching fractions, CP asymmetry, and isospin asymmetry for $B \to \rho\gamma$ decays using Belle and Belle II data

I. Adachi, K. Adamczyk, L. Aggarwal, H. Aihara, N. Akopov, A. Aloisio, N. Anh Ky, D. M. Asner, H. Atmacan, T. Aushev, V. Aushev, M. Aversano, R. Ayad, V. Babu, H. Bae, S. Bahinipati, P. Bambade, Sw. Banerjee, S. Bansal, M. Barrett, J. Baudot, A. Baur, A. Beaubien, F. Becherer, J. Becker, J. V. Bennett, F. U. Bernlochner, V. Bertacchi, M. Bertemes, E. Bertholet, M. Bessner, S. Bettarini, B. Bhuyan, F. Bianchi, L. Bierwirth, T. Bilka, S. Bilokin, D. Biswas, A. Bobrov, D. Bodrov, A. Bolz, A. Bondar, A. Bozek, M. Bračko, P. Branchini, R. A. Briere, T. E. Browder, A. Budano, S. Bussino, M. Campajola, L. Cao, G. Casarosa, C. Cecchi, J. Cerasoli, M.-C. Chang, P. Chang, R. Cheaib, P. Cheema, B. G. Cheon, K. Chilikin, K. Chirapatpimol, H.-E. Cho, K. Cho, S.-K. Choi, S. Choudhury, L. Corona, S. Das, F. Dattola, E. De La Cruz-Burelo, S. A. De La Motte, G. De Nardo, M. De Nuccio, G. De Pietro, R. de Sangro, M. Destefanis, R. Dhamija, A. Di Canto, F. Di Capua, J. Dingfelder, Z. Doležal, T. V. Dong, M. Dorigo, K. Dort, D. Dossett, S. Dreyer, S. Dubey, G. Dujany, P. Ecker, M. Eliachevitch, D. Epifanov, P. Feichtinger, T. Ferber, D. Ferlewicz, T. Fillinger, C. Finck, G. Finocchiaro, A. Fodor, F. Forti, A. Frey, B. G. Fulsom, A. Gabrielli, E. Ganiev, M. Garcia-Hernandez, R. Garg, G. Gaudino, V. Gaur, A. Gaz, A. Gellrich, G. Ghevondyan, D. Ghosh, H. Ghumaryan, G. Giakoustidis, R. Giordano, A. Giri, A. Glazov, B. Gobbo, R. Godang, O. Gogota, P. Goldenzweig, W. Gradl, T. Grammatico, E. Graziani, D. Greenwald, Z. Gruberová, T. Gu, Y. Guan, K. Gudkova, S. Halder, Y. Han, T. Hara, H. Hayashii, S. Hazra, M. T. Hedges, A. Heidelbach, I. Heredia de la Cruz, M. Hernández Villanueva, T. Higuchi, M. Hoek, M. Hohmann, P. Horak, C.-L. Hsu, T. Humair, T. Iijima, K. Inami, N. Ipsita, A. Ishikawa, R. Itoh, M. Iwasaki, P. Jackson, W. W. Jacobs, E.-J. Jang, Q. P. Ji, S. Jia, Y. Jin, K. K. Joo, H. Junkerkalefeld, D. Kalita, A. B. Kaliyar, J. Kandra, K. H. Kang, G. Karyan, T. Kawasaki, F. Keil, C. Kiesling, C.-H. Kim, D. Y. Kim, K.-H. Kim, Y.-K. Kim, H. Kindo, K. Kinoshita, P. Kodyš, T. Koga, S. Kohani, K. Kojima, A. Korobov, S. Korpar, E. Kovalenko, R. Kowalewski, T. M. G. Kraetzschmar, P. Križan, P. Krokovny, T. Kuhr, J. Kumar, M. Kumar, R. Kumar, K. Kumara, T. Kunigo, A. Kuzmin, Y.-J. Kwon, S. Lacaprara, Y.-T. Lai, T. Lam, L. Lanceri, J. S. Lange, M. Laurenza, K. Lautenbach, R. Leboucher, F. R. Le Diberder, M. J. Lee, D. Levit, P. M. Lewis, C. Li, L. K. Li, Y. Li, Y. B. Li, J. Libby, M. H. Liu, Q. Y. Liu, Z. Q. Liu, D. Liventsev, S. Longo, T. Lueck, C. Lyu, Y. Ma, M. Maggiora, S. P. Maharana, R. Maiti, S. Maity, G. Mancinelli, R. Manfredi, E. Manoni, M. Mantovano, D. Marcantonio, S. Marcello, C. Marinas, L. Martel, C. Martellini, A. Martini, T. Martinov, L. Massaccesi, M. Masuda, D. Matvienko, S. K. Maurya, J. A. McKenna, R. Mehta, F. Meier, M. Merola, F. Metzner, C. Miller, M. Mirra, K. Miyabayashi, H. Miyake, R. Mizuk, G. B. Mohanty, N. Molina-Gonzalez, S. Mondal, S. Moneta, H.-G. Moser, M. Mrvar, R. Mussa, I. Nakamura, K. R. Nakamura, M. Nakao, Y. Nakazawa, A. Narimani Charan, M. Naruki, D. Narwal, Z. Natkaniec, A. Natochii, L. Nayak, M. Nayak, G. Nazaryan, M. Neu, C. Niebuhr, S. Nishida, S. Ogawa, Y. Onishchuk, H. Ono, P. Oskin, F. Otani, P. Pakhlov, G. Pakhlova, A. Panta, S. Pardi, K. Parham, H. Park, S.-H. Park, A. Passeri, S. Patra, S. Paul, T. K. Pedlar, R. Peschke, R. Pestotnik, M. Piccolo, L. E. Piilonen, G. Pinna Angioni, P. L. M. Podesta-Lerma, T. Podobnik, S. Pokharel, C. Praz, S. Prell, E. Prencipe, M. T. Prim, H. Purwar, P. Rados, G. Raeuber, S. Raiz, N. Rauls, M. Reif, S. Reiter, M. Remnev, I. Ripp-Baudot, G. Rizzo, S. H. Robertson, M. Roehrken, J. M. Roney, A. Rostomyan, N. Rout, G. Russo, D. A. Sanders, S. Sandilya, L. Santelj, Y. Sato, V. Savinov, B. Scavino, C. Schmitt, C. Schwanda, A. J. Schwartz, M. Schwickardi, Y. Seino, A. Selce, K. Senyo, J. Serrano, M. E. Sevior, C. Sfienti, W. Shan, C. P. Shen, X. D. Shi, T. Shillington, T. Shimasaki, J.-G. Shiu, D. Shtol, A. Sibidanov, F. Simon, J. B. Singh, J. Skorupa, R. J. Sobie, M. Sobotzik, A. Soffer, A. Sokolov, E. Solovieva, S. Spataro, B. Spruck, M. Starič, P. Stavroulakis, S. Stefkova, R. Stroili, M. Sumihama, K. Sumisawa, W. Sutcliffe, H. Svidras, M. Takizawa, U. Tamponi, S. Tanaka, K. Tanida, F. Tenchini, O. Tittel, R. Tiwary, D. Tonelli, E. Torassa, K. Trabelsi, I. Tsaklidis, M. Uchida, I. Ueda, Y. Uematsu, T. Uglov, K. Unger, Y. Unno, K. Uno, S. Uno, P. Urquijo, Y. Ushiroda, S. E. Vahsen, R. van Tonder, K. E. Varvell, M. Veronesi, A. Vinokurova, V. S. Vismaya, L. Vitale, V. Vobbilisetti, R. Volpe, B. Wach, M. Wakai, S. Wallner, E. Wang, M.-Z. Wang,

X. L. Wang, Z. Wang, A. Warburton, S. Watanuki, C. Wessel, J. Wiechczynski, E. Won, X. P. Xu, B. D. Yabsley, S. Yamada, W. Yan, S. B. Yang, J. Yelton, J. H. Yin, K. Yoshihara, C. Z. Yuan, L. Zani, B. Zhang, Y. Zhang, V. Zhilich, Q. D. Zhou, X. Y. Zhou, and V. I. Zhukova

(Dated: March 14, 2025)

We present measurements of $B^+ \to \rho^+\gamma$ and $B^0 \to \rho^0\gamma$ decays using a combined data sample of 772×10^6 $B\overline{B}$ pairs collected by the Belle experiment and 387×10^6 $B\overline{B}$ pairs collected by the Belle II experiment in e^+e^- collisions at the $\Upsilon(4S)$ resonance. After an optimized selection, a simultaneous fit to the Belle and Belle II data sets yields 114 ± 12 $B^+ \to \rho^+\gamma$ and 99 ± 12 $B^0 \to \rho^0\gamma$ decays. The measured branching fractions are $(13.1^{+2.0+1.3}_{-1.9-1.2}) \times 10^{-7}$ and $(7.6 \pm 1.3^{+1.0}_{-0.8}) \times 10^{-7}$ for $B^+ \to \rho^+\gamma$ and $B^0 \to \rho^0\gamma$ decays, respectively, where the first uncertainty is statistical and the second is systematic. We also measure the isospin asymmetry $A_{\rm I}(B \to \rho\gamma) = (10.9^{+11.2+7.8}_{-11.7-7.3})\%$ and the direct CP asymmetry $A_{CP}(B^+ \to \rho^+\gamma) = (-8.2 \pm 15.2^{+2.0}_{-1.3})\%$.

I. INTRODUCTION

Flavor-changing neutral-current (FCNC) processes are sensitive probes of physics beyond the standard model (SM) [1–6]. These decays are forbidden at the tree level and must proceed via an internal loop (or "penguin") amplitude, making them particularly sensitive to beyond-the-SM contributions. Among FCNC decays, radiative decays such as $B \to K^*\gamma$ and $B \to \rho\gamma$ are especially attractive, as these two-body decays with a high-momentum photon are straightforward to reconstruct at an e^+e^- experiment.

The $B \to \rho\gamma$ decay proceeds via a $b \to d$ loop amplitude and has a measured branching fraction one order of magnitude smaller than that for $B \to K^*\gamma$, which proceeds via a $b \to s$ loop amplitude. This difference is attributed to both loops being dominated by the heavy top quark; thus, the $b \to s$ amplitude is proportional to the Cabibbo-Kobayashi-Maskawa (CKM) matrix element V_{ts}, while the $b \to d$ amplitude is proportional to the five-times-smaller CKM element V_{td}. Measuring these decays provides information about the magnitudes $|V_{ts}|$ and $|V_{td}|$. In addition, beyond-the-SM contributions can contribute to the decay amplitudes. Such contributions could be easier to identify in $B \to \rho\gamma$ decays due to the smaller SM rate. The decay $B \to \rho\gamma$ was first observed by Belle experiment [7] in 2006 and later confirmed by *BABAR* experiment [8]. Both experiments subsequently made more precise measurements of the branching fractions with larger data sets: 657×10^6 $B\overline{B}$ pairs for Belle [9] and 465×10^6 $B\overline{B}$ pairs for *BABAR* [10].

In addition to the branching fraction, another observable of interest is the CP asymmetry

$$A_{CP}(B \to \rho\gamma) = \frac{\Gamma\left(\overline{B} \to \bar{\rho}\gamma\right) - \Gamma\left(B \to \rho\gamma\right)}{\Gamma\left(\overline{B} \to \bar{\rho}\gamma\right) + \Gamma\left(B \to \rho\gamma\right)}. \quad (1)$$

Within the context of QCD factorization, A_{CP} is predicted to be significant: about -12% [5]. Thus, measuring A_{CP} provides a test of factorization. Also, beyond-the-SM amplitudes can shift the value of A_{CP}, and measuring A_{CP} could indicate the presence of such contributions.

A third observable for $B \to \rho\gamma$ is the CP-averaged isospin asymmetry $\langle A_{\rm I}\rangle = \left(A_{\rm I}^b + A_{\rm I}^{\bar{b}}\right)/2$, with

$$A_{\rm I}^b = \frac{c_\rho^2\Gamma\left(\overline{B}^0 \to \rho^0\gamma\right) - \Gamma\left(B^- \to \rho^-\gamma\right)}{c_\rho^2\Gamma\left(\overline{B}^0 \to \rho^0\gamma\right) + \Gamma\left(B^- \to \rho^-\gamma\right)} \quad (2)$$

and $A_{\rm I}^{\bar{b}}$ defined similarly but with CP-conjugate modes. The factor $c_\rho = \sqrt{2}$ results from the quark content of the ρ^0 meson (i.e., a Clebsch-Gordan coefficient). The asymmetry $\langle A_{\rm I}^{\rm SM}\rangle$ is predicted to be close to that of $B \to K^*\gamma$ and to equal $(5.2 \pm 2.8)\%$, where a large source of uncertainty is the renormalization scale used to calculate Wilson coefficients [11]. As for A_{CP}, beyond-the-SM contributions can affect $\langle A_{\rm I}\rangle$ [2–5]. Only the isospin asymmetry with CP-averaged decay rates, $A_{\rm I}$, has been measured to date:

$$A_{\rm I} = \frac{c_\rho^2\Gamma(\overset{(-)}{B^0} \to \rho^0\gamma) - \Gamma(B^\pm \to \rho^\pm\gamma)}{c_\rho^2\Gamma(\overset{(-)}{B^0} \to \rho^0\gamma) + \Gamma(B^\pm \to \rho^\pm\gamma)}, \quad (3)$$

where B^0 and $\overline{B}^0$ are summed and B^+ and B^- are summed in both the numerator and the denominator. The observable $A_{\rm I}$ equals $\langle A_{\rm I}\rangle$ if the CP asymmetry is the same for $B^+ \to \rho^+\gamma$ and $B^0 \to \rho^0\gamma$ decays. The current world average of isospin asymmetry measurements, $A_{\rm I}^{\rm exp}(\rho\gamma) = (30^{+16}_{-13})\%$ [12], is about two standard deviations above the SM expectation.

Here we report measurements of $B \to \rho\gamma$ decays performed using both Belle and Belle II data sets. The signal decay modes are $B^+ \to \rho^+\left(\to \pi^0\pi^+\right)\gamma$ and $B^0 \to \rho^0\left(\to \pi^+\pi^-\right)\gamma$ [13]. We use the full Belle data set corresponding to 711 fb^{-1} taken at the $\Upsilon(4S)$ resonance energy (on-resonance) and containing $(772 \pm 11) \times 10^6$ $B\overline{B}$ pairs. In addition, we use a 362 fb^{-1} Belle II data set collected from 2019–2022 containing $(387 \pm 6) \times 10^6$ $B\overline{B}$ pairs. We use off-resonance data sets collected at an energy 60 MeV below the $\Upsilon(4S)$ resonance, to study continuum background processes $e^+e^- \to q\bar{q}$, where $q = u, d, s, c$. The off-resonance data samples correspond to 89.5 fb^{-1} and 42.3 fb^{-1} for Belle and Belle II, respectively.

This paper is organized as follows. Section II introduces the Belle and Belle II detectors followed by the description of the data and simulated samples. The event selection and reconstruction of the decays are described in section III. The methods to suppress background are presented in section IV. Section V explains the fitting procedure to extract signal yields. The systematic uncertainties are discussed in section VI. The results are presented in section VII.

II. DETECTORS AND DATA SETS

The Belle detector [14, 15] was a large-solid-angle spectrometer that operated at the KEKB asymmetric-energy e^+e^- (3.5 GeV on 8.0 GeV) collider [16, 17] from 1999 to 2010. The detector consisted of a silicon vertex detector and a central drift chamber (CDC) for reconstructing trajectories of charged particles (tracks), an array of aerogel Cherenkov counters (ACC) and time-of-flight scintillation counters (TOF) for identifying charged particles, and an electromagnetic CsI(Tl) crystal calorimeter (ECL) for identifying photons and electrons. These detectors were surrounded by a superconducting solenoid coil providing a magnetic field of 1.5 T. An iron flux return yoke located outside the coil was instrumented with resistive-plate chambers to detect K_L^0 mesons and identify muons.

The Belle II detector [18] is an upgrade of the Belle detector and operates at the SuperKEKB e^+e^- collider. The energies of electron and positron beams are 7.0 GeV and 4.0 GeV, respectively. The vertex detector consists of pixel sensors and double-sided silicon strips. The Belle II CDC is surrounded by two types of Cherenkov light detector systems used for particle identification: a time-of-propagation detector (TOP) for the barrel region (32.2° to 128.7°), and an aerogel ring-imaging Cherenkov detector (ARICH) for the forward endcap region (12.4° to 31.4°). The Belle ECL is re-used in Belle II along with the solenoid and the iron flux return yoke. For both Belle and Belle II, the z axis is defined as the central axis of the solenoid, with the positive direction being very close to the direction of the electron beam.

Monte Carlo simulated samples are used to optimize selection criteria, study sources of backgrounds, calculate reconstruction efficiencies, and determine probability density functions (PDFs) used for fitting the data. We use EvtGen [19] to generate $e^+e^- \to B\overline{B}$ pairs. In addition, we use Pythia 8.2 [27] for the Belle II sample. We simulate continuum background events using Pythia 6.4 [25] for the analysis of Belle data, and KKMC [26] for hard scattering followed by Pythia 8.2 [27] for hadronization in Belle II. We simulate the effects of final state radiation by Photos [28] for both Belle and Belle II. The detector response is based on GEANT3 [20] and GEANT4 [21] for Belle and Belle II data, respectively. We use simulated samples of 2×10^6 signal events and more than 1 ab^{-1} of background events for our studies. The data and simulation are processed using the Belle II analysis software framework [22–24].

III. EVENT SELECTION

The triggers of Belle and Belle II use either the number of tracks, or ECL energy depositions (clusters), or the total energy of all clusters. The trigger efficiency for signal events is almost 100%.

In the offline analysis, most of the selection criteria used for Belle and Belle II are similar; however, certain criteria are adjusted to account for the improved performance of the upgraded detector. A high energy primary photon ($\gamma_{\rm prim}$) candidate is reconstructed from an ECL cluster not associated with any track. Only ECL clusters whose polar angle θ is in the barrel region are considered. The energy of the primary photon candidate in the e^+e^- center-of-mass (c.m.) frame, denoted E^*_γ, is required to be in the range $(1.8, 2.8)$ GeV. All quantities with asterisks are calculated in the e^+e^- c.m. frame. For Belle, we require $E_9/E_{25} > 0.95$ to select a cluster shape consistent with an electromagnetic shower, where E_9/E_{25} is defined as the ratio of energy deposits within a 3×3 array of CsI(Tl) crystals and within a 5×5 array, both centered on the crystal with the highest energy. For Belle II, we require $E_9/E_{21} > 0.95$, where E_{21} is defined similarly to E_{25} but with energy deposits at the four corners of the 5×5 array removed. We also define for Belle II a cluster second moment $S \equiv \Sigma_i w_i E_i r_i^2/\Sigma_i w_i E_i$, where E_i is the energy deposited in the ith crystal, and r_i is the distance in the plane perpendicular to the shower axis from the center of the cluster to the center of the ith crystal [31]. The energies are weighted by factors w_i ranging from 0.0–1.0 that account for a crystal energy being shared among overlapping clusters. The sum is taken over all crystals in a cluster. To reject clusters resulting from hadron showers, we require that there be at least eight crystals in a cluster. To better identify the primary photon cluster, we require $S < 1.5$ cm^2.

Track candidates are required to satisfy $dr < 0.5$ cm and $|dz| < 2$ cm, where dr and dz are transverse and longitudinal impact parameters, respectively. We select π^+ candidates from tracks by requiring $\mathcal{R}_{\pi/K} = \mathcal{L}_\pi/(\mathcal{L}_\pi + \mathcal{L}_K) > 0.6$, where $\mathcal{L}_{\pi(K)}$ is the likelihood for a pion (kaon) hypothesis. These likelihoods are based on information from the CDC, ACC, and TOF detectors in Belle, and from the CDC, TOP, and ARICH detectors in Belle II.

Neutral π^0 mesons are reconstructed via $\pi^0 \to \gamma\gamma$ decays. In Belle data, π^0 mesons are reconstructed using two photons, each with energy greater than 50 MeV. We require the invariant mass of the two photons to satisfy 119 MeV/c^2 $< M(\gamma\gamma) <$ 151 MeV/c^2. In Belle II data, the energy thresholds of the daughter photons depend on the region in the ECL. For the barrel region, the daughter photons are required to have energies greater than 30 MeV, while for the forward and backward endcap regions we use thresholds of 80 MeV and 60 MeV, respectively. In addition, the daughter photons must satisfy the condition $\Sigma w_i > 1.5$. The invariant mass of the two photons in Belle II is required to be in the range $120\ \mathrm{MeV}/c^2 < M(\gamma\gamma) < 145\ \mathrm{MeV}/c^2$.

We reconstruct $\rho^0 \to \pi^+\pi^-$ and $\rho^+ \to \pi^+\pi^0$ candidates by requiring that the invariant mass of the pion pair be in the range $[0.64, 0.90]\ \mathrm{GeV}/c^2$ for Belle data, and the range $[0.65, 0.90]\ \mathrm{GeV}/c^2$ for Belle II data. The slight difference in the lower edge of these ranges is due to a slight shift in the $M(\pi^+\pi^0)$ spectrum for Belle II. A B candidate is subsequently reconstructed by combining a ρ candidate with a γ_{prim} candidate.

To remove low multiplicity and $q\overline{q}$ events, we require at least two tracks in the event and that the ratio of the second to zeroth Fox-Wolfram moments [30] be less than 0.7. To fit for the signal yield, we define two observables: the beam-energy-constrained mass $M_{\mathrm{bc}} \equiv \sqrt{(E^*_{\mathrm{beam}}/c^2)^2 - |\mathbf{p}^*_B/c|^2}$, and the energy difference $\Delta E \equiv E^*_B - E^*_{\mathrm{beam}}$, where E_{beam} is the beam energy and E_B and p_B are the reconstructed energy and momentum, respectively, of the signal B candidate. For the $B^0 \to \rho^0\gamma$ mode, we improve the resolution in M_{bc} by substituting, for the magnitude of the photon momentum, the difference between the beam energy and the energy of the ρ^0 candidate: $\vec{\boldsymbol{p}}^*_{B^0} \to \vec{\boldsymbol{p}}^*_{\rho^0} + \left(\vec{\boldsymbol{p}}^*_{\gamma}/|\vec{\boldsymbol{p}}^*_{\gamma}|\right)\left(E^*_{\mathrm{beam}} - E^*_{\rho^0}\right)/c$, where $E^*_{\rho^0}$ and $\vec{\boldsymbol{p}}^*_{\rho^0}$ are the energy and momentum, respectively, of the ρ^0 candidate, and $\vec{\boldsymbol{p}}^*_{\gamma}$ is the momentum of the γ_{prim} candidate. According to MC simulation, this modification reduces the width of the M_{bc} distribution by 18%. We retain signal candidates that satisfy $M_{\mathrm{bc}} > 5.2\ \mathrm{GeV}/c^2$ and $|\Delta E| < 0.3$ GeV. In addition, we define a variable $M(K\pi)$, which is the invariant mass of the ρ candidate calculated assuming that one of the charged pions is a kaon. For $\rho^0 \to \pi^+\pi^-$ decays, the substitution of the kaon mass for the pion mass is applied to the pion with the lower value of $\mathcal{R}_{\pi/K}$. This allows us to distinguish $B \to \rho\gamma$ from $B \to K^*\gamma$, which peaks in the $K^*(892)^0$ mass region. We retain events in the wide range $M(K\pi) \in (0.80, 1.50)\ \mathrm{GeV}/c^2$ and use $M(K\pi)$ in the signal extraction procedure to better discriminate $B \to K^*\gamma$ decays from the signal. To reduce combinatorial background arising from other $B\overline{B}$ events, the B meson candidate must also satisfy $|\cos\theta_h| < 0.8$, where θ_h is the angle in the B rest frame between the momentum of γ_{prim} and the negative of the boost direction of the laboratory frame. For correctly reconstructed signal decays, the $|\cos\theta_h|$ distribution is uniform, while for combinatorial background, the distribution tends to peak at $|\cos\theta_h| \approx 1$. After applying the selection criteria listed above, 12.3% (3.0%) of events have multiple $B^+ \to \rho^+\gamma$ ($B^0 \to \rho^0\gamma$) candidates. For such multiple candidate events, the average multiplicity is 2.3 for both B^+ and B^0 decays. To minimize potential bias, we select one candidate randomly.

To assess the quality of the simulation, we compare its predictions with data using two control samples, $B \to \overline{D}\pi^+$ and $B \to K^*\gamma$ decays. These control sample studies are described in the following sections. We reconstruct both $\overline{D}^0 \to K^+\pi^-$ and $D^- \to K^+\pi^-\pi^-$ decays, requiring that the invariant masses be in the ranges $1.85\ \mathrm{GeV}/c^2 < M(K^+\pi^-) < 1.88\ \mathrm{GeV}/c^2$ and $1.86\ \mathrm{GeV}/c^2 < M(K^+\pi^-\pi^-) < 1.88\ \mathrm{GeV}/c^2$. The K^* mesons are reconstructed via $K^{*+} \to K^+\pi^0$ and $K^{*0} \to K^+\pi^-$ decays, where the charged kaon is required to have $\mathcal{R}_{K/\pi} > 0.6$ and the π^0 and π^- must satisfy the same criteria as applied to signal $B \to \rho^0\gamma$ decays. The invariant mass of the $K\pi$ meson pair must satisfy $0.817\ \mathrm{GeV}/c^2 < M(K^+\pi^{-(0)}) < 0.967\ \mathrm{GeV}/c^2$.

IV. BACKGROUND SUPPRESSION

After applying the above selection criteria, the main remaining source of background is $q\overline{q}$ events, where the candidate γ_{prim} results from an asymmetric $\pi^0 \to \gamma\gamma$ or $\eta \to \gamma\gamma$ decay. In this case, one of the photons has much higher energy than the other. To reduce this background, we use two boosted decision trees: a dedicated $\pi^0(\eta)$ veto and one for $q\overline{q}$ suppression.

A. $\pi^0(\eta)$ veto

For the π^0 and η veto, we pair γ_{prim} with other photons in the event to reconstruct $\pi^0 \to \gamma\gamma$ and $\eta \to \gamma\gamma$ decays. If such a candidate is identified, the γ_{prim} candidate is removed. The energy of the photon with which γ_{prim} is paired (γ_{soft}) must exceed a polar-angle-dependent threshold. For Belle II data, we require that the sum of crystal weights w_i for the γ_{soft} cluster be at least two, and that this cluster be reconstructed in time with the event trigger. The probability of a correctly reconstructed $\pi^0(\eta)$ is calculated using a boosted decision tree (BDT_v) trained using simulated events. The BDT_v uses up to eight input variables: (1) the invariant mass of the two photons $M(\gamma_{\mathrm{prim}}\gamma_{\mathrm{soft}})$; (2) the γ_{soft} energy; (3) the γ_{soft} polar angle; (4) Σw_i for the γ_{soft} cluster; (5) the γ_{soft} $E_9/E_{25(21)}$; (6) the cosine of the angle in the $\pi^0(\eta)$ rest frame between the momentum of γ_{prim} and the negative of the boost direction of the laboratory frame; (7) the distance between the ECL cluster of γ_{soft} and the nearest track extrapolated to the ECL; and (8) the output of a multivariate classifier based on Zernike moments of the γ_{soft} shower [32]. These moments are defined in the plane perpendicular to the shower direction. Requirements (7) and (8) are not applied to Belle data, while for Belle II data, variables (4), (5), and (8) are used only for the η veto.

The BDT_v value is calculated for all γ_{soft} candidates. Among all $\gamma_{\mathrm{prim}}\gamma_{\mathrm{soft}}$ pairs, the one with the highest BDT_v value is selected. The background in which the γ_{prim} originates from $\pi^0(\eta) \to \gamma\gamma$ decays tends to peak at one. Selection criteria on the BDT_v output are optimized to maximize the signal significance, $n_s/\sqrt{n_s + n_b}$, where $n_{s(b)}$ is the number of simulated signal (background) events after the BDT_v selection in a signal-enriched region defined as $M_{\rm bc} > 5.27$ GeV/c^2, -0.20 GeV $< \Delta E <$ 0.10 GeV, and $M(K\pi) > 0.92$ GeV/c^2. The optimized selection for BDT_v rejects about 75% (82%) of $q\bar{q}$ background for Belle (Belle II) data, while retaining about 83% (89%) of signal decays.

The signal efficiency is calibrated using a $B \to \overline{D}\pi^+$ control sample. Figure 1 shows the BDT_v distributions for data and MC-simulated events for the control sample. There is good agreement between the data and MC distributions for Belle data, but small differences are observed for Belle II data. The π^+ momentum is scaled by a factor 1.087 to match the momentum of $\gamma_{\rm prim}$, and the mass $M(\pi\gamma_{\rm soft})$ is used in place of $M(\gamma_{\rm prim}\gamma_{\rm soft})$. Due to isolation criteria applied to the $\gamma_{\rm prim}$ candidate, the distribution of $M(\pi\gamma_{\rm soft})$ differs from that of $M(\gamma_{\rm prim}\gamma_{\rm soft})$; to correct for this, the $B \to \overline{D}\pi^+$ events are weighted such that these distributions match. After this weighting, the BDT_v distributions show improved agreement with MC-simulated $B \to \rho\gamma$ events. The small difference in signal efficiency before and after this weighting is also taken as a systematic uncertainty.

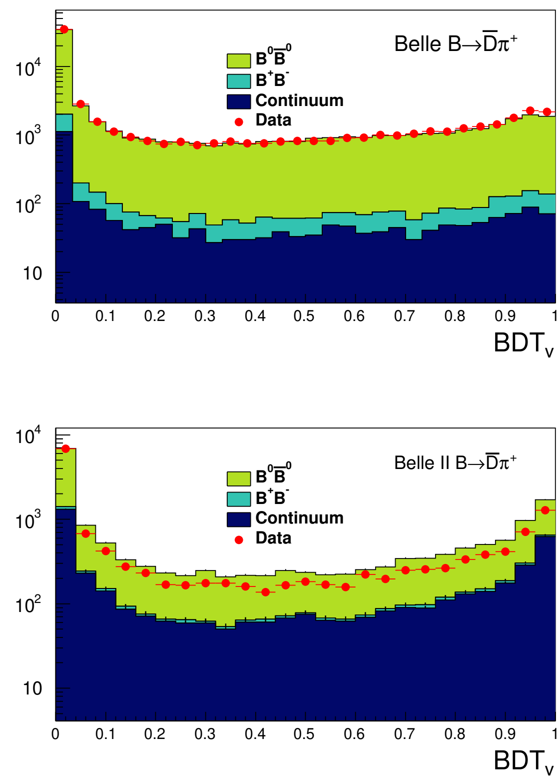

FIG. 1: Distributions of BDT_v for data (red plot) and simulation (stack histogram) for Belle (top) and Belle II (bottom).

B. $q\bar{q}$ suppression

To reduce the remaining contamination from continuum background, we introduce another boosted decision tree classifier ($BDT_{q\bar{q}}$) that relies on differences in event shapes between $B\overline{B}$ and continuum $q\bar{q}$ events. The variables used in $BDT_{q\bar{q}}$ are as follows: the cosine of the angle between the thrust axis of the signal B candidate and the thrust axis of the rest of the event $\cos\theta_{T_BT_O}$ [33]; modified Fox-Wolfram moments [30, 34]; the outputs of the B flavor-tagging algorithms of Belle [35] and Belle II [36]; the difference between the z coordinates of the signal and the companion B decay vertices (Δz); the distance-of-closest-approach between the signal π^+ track and the companion B decay vertex; the sphericity of non-signal particles in the event [37]; and the cosine of the polar angle of the signal B. The $\cos\theta_{T_BT_O}$ variable is the most discriminating. The flavor-tagging algorithm outputs two quantities: the flavor tag q ($= \pm1$), and a quality factor r that ranges from zero for no flavor discrimination to one for unambiguous flavor assignment. The $BDT_{q\bar{q}}$ training uses simulated $B \to \rho\gamma$ and continuum events. The training is performed separately for $B^+ \to \rho^+\gamma$ and $B^0 \to \rho^0\gamma$ decays, and for Belle and Belle II data. The requirements on the $BDT_{q\bar{q}}$ output are chosen to maximize the signal significance, separately for three ranges of the flavor-tagging quality r: $(0, 0.4)$, $(0.4, 0.825)$, and $(0.825, 1)$. All requirements are greater than 0.95. The signal efficiency is estimated from simulation and corrected for possible differences between data and simulation using the ratio of efficiencies between data and simulation for the $B \to K^*\gamma$ control samples. These correction factors range from 0.96 to 1.10. The signal efficiencies in Belle data for the $BDT_{q\bar{q}}$ requirement are 30% and 40% for B^+ and B^0 decays, respectively. For Belle II data, the corresponding efficiencies are 45% and 52%. The higher signal efficiencies for Belle II are mainly due to improved resolution on Δz and the distance-of-closest-approach between the $\pi^\pm$ track and the companion B decay vertex. This improved resolution results from the additional pixel layers of the Belle II vertex detector.

V. SIGNAL EXTRACTION

To measure the $B \to \rho\gamma$ branching fractions and asymmetries $A_{\rm I}$ and A_{CP}, we perform an extended unbinned maximum likelihood fit to the observables $M_{\rm bc}$, ΔE, and $M(K\pi)$. We simultaneously fit six independent data sets: B^+, B^-, and $(B^0 + \overline{B}^0)$ candidates combined, for Belle and Belle II data. In the fit, we model four components: signal, $B \to K^*\gamma$, $B\overline{B}$ background, and $q\bar{q}$ background. The probability density functions (PDFs) used for these components are as follows.

For MC-simulated signal decays, $M_{\rm bc}$, ΔE, and $M(K\pi)$ are found to be essentially uncorrelated, and the PDF is taken to be the product of separate functions for each. We model both the $M_{\rm bc}$ and ΔE distributions with Crystal Ball functions [38], and the $M(K\pi)$ distribution with a Novosibirsk function [40] convolved with a Gaussian. For $B \to K^*\gamma$ background, $M_{\rm bc}$, ΔE, and $M(K\pi)$ are correlated, and we use a three-dimensional histogram PDF. For $B\overline{B}$ background, we again use the product of three one-dimensional functions: the sum of a Crystal Ball function and ARGUS function [39] for $M_{\rm bc}$, an exponential function for ΔE, and a histogram PDF for $M(K\pi)$. Finally, for $q\overline{q}$ background, we use the product of an ARGUS function for $M_{\rm bc}$, a quadratic Chebychev polynomial for ΔE, and a Novosibirsk function convolved with a Gaussian for $M(K\pi)$.

The shape parameters of the ΔE distribution for $q\overline{q}$ background are floated in the fit, while all other PDF shape parameters are fixed to values obtained from MC simulation. To account for possible differences between data and simulation, the $M_{\rm bc}$ and ΔE distributions for signal decays are corrected according to small differences observed between data and simulation for the $B \to K^*\gamma$ control samples. Similarly, the parameters for the $M_{\rm bc}$ and $M(K\pi)$ distributions of $q\overline{q}$ background are corrected according to small differences observed between data and simulation in the sideband region $BDT_{q\overline{q}} \in [0.6, 0.9]$. In addition to these fixed shapes, we also fix the yields of $B \to K^*\gamma$ and $B\overline{B}$ backgrounds to expectations based on MC simulation.

With the above PDFs, we perform two fits. We first fit directly for parameters D, $A_{\rm I}$, and A_{CP}, defined as

$$D = c_\rho^2 \frac{\tau_{B^\pm}}{\tau_{B^0}} \mathcal{B}(\overset{(-)}{B^0} \to \rho^0\gamma) + \mathcal{B}\left(B^\pm \to \rho^\pm\gamma\right), \quad (4)$$

$$A_{\rm I} = \frac{c_\rho^2 \frac{\tau_{B^\pm}}{\tau_{B^0}} \mathcal{B}(\overset{(-)}{B^0} \to \rho^0\gamma) - \mathcal{B}\left(B^\pm \to \rho^\pm\gamma\right)}{D}, \quad (5)$$

and

$$A_{CP} = \frac{N_{B^-} - N_{B^+}}{N_{B^-} + N_{B^+}}, \quad (6)$$

where $\tau_{B^\pm}/\tau_{B^0} = 1.076 \pm 0.004$ [12] is the ratio of $B^\pm$ to B^0 lifetimes.

The relationship between the number of signal events (N_i) and the branching fractions in Eq. 5 and 6 is given by

$$\mathcal{B}(B^{\pm(0)} \to \rho^{\pm(0)}\gamma) = \frac{N_{B^-(\overline{B}^0)} + N_{B^+(B^0)}}{2N_{B\overline{B}} f_{+-(00)} \epsilon^{\pm(0)}}. \quad (7)$$

Here, $N_{B\overline{B}}$ is the number of $B\overline{B}$ pairs and equals $(771.6 \pm 10.6) \times 10^6$ for Belle and $(378.5 \pm 5.8) \times 10^6$ for Belle II; $f_{+-}/f_{00} = 1.065 \pm 0.052$ [42, 43] is the production ratio of B^+B^- to $B^0\overline{B}^0$ pairs at an e^+e^- center-of-mass energy corresponding to the $\Upsilon(4S)$ resonance; and $\epsilon^\pm$ and ϵ^0 are reconstruction efficiencies for $B^\pm \to \rho^\pm\gamma$ and $B^0 \to \rho^0\gamma$, respectively. The efficiencies of $B^+ \to \rho^+\gamma$ and $B^- \to \rho^-\gamma$ decays are consistent with each other and taken to be identical. The signal efficiencies $\epsilon^\pm$ and ϵ^0 for the Belle (Belle II) sample are 5.5% and 10.3% (11.0% and 14.9%), respectively. The higher efficiency for Belle II is due mainly to the improved performance of the BDT_v and $BDT_{q\overline{q}}$ algorithms. After this first fit, we perform a second fit directly for $\mathcal{B}\left(B^+ \to \rho^+\gamma\right)$ and $\mathcal{B}\left(B^- \to \rho^-\gamma\right)$ to obtain their uncertainties (rather than unfolding them from the first fit results, accounting for correlations). The distributions of $M_{\rm bc}$, ΔE, and $M(K\pi)$ are shown in Figs. 2–4 along with projections of the fit result.

Using Eqs. 4-7, we extract the signal yields; these are listed in Table I along with the corresponding reconstruction efficiencies and the fitted yields of $q\overline{q}$ background. The overall signal yields in the full fitted region are 114 ± 12 $B^\pm \to \rho^\pm\gamma$ decays and 99 ± 12 $B^0 \to \rho^0\gamma$ decays. As a cross-check, we fit for the branching fractions using only Belle data; our results are in agreement with the previous Belle measurement [9].

TABLE I: Efficiency (ϵ), signal yield ($N_{\rho\gamma}$) and continuum background yield ($N_{q\overline{q}}$) from Belle (711 fb^{-1}) and Belle II (362 fb^{-1}) data. The uncertainties for $N_{\rho\gamma(q\overline{q})}$ are statistical only.

Mode	ϵ [%]	$N_{\rho\gamma}$	$N_{q\overline{q}}$
Belle $B^+ \to \rho^+\gamma$	5.5 ± 0.5	31 ± 6	400 ± 21
Belle $B^- \to \rho^-\gamma$	5.5 ± 0.5	26 ± 6	369 ± 21
Belle $B^0 \to \rho^0\gamma$	10.3 ± 0.4	58 ± 10	1307 ± 38
Belle II $B^+ \to \rho^+\gamma$	11.0 ± 1.1	30 ± 6	552 ± 25
Belle II $B^- \to \rho^-\gamma$	11.0 ± 1.1	26 ± 6	549 ± 25
Belle II $B^0 \to \rho^0\gamma$	14.9 ± 0.5	41 ± 7	1114 ± 35

VI. SYSTEMATIC UNCERTAINTIES

The various sources of systematic uncertainty are listed in Table II and estimated as follows.

The systematic uncertainty arising from particle reconstruction consists of several parts. The uncertainty related to photon detection is measured in Belle using $e^+e^- \to e^+e^-\gamma$ (radiative Bhabha) events and in Belle II using $e^+e^- \to \mu^+\mu^-\gamma$ events; the resulting uncertainties are 2% and 1%, respectively. The uncertainty due to π^+ identification is measured in Belle (0.7%) and Belle II (0.3%) using a sample of $D^{*+} \to D^0(\to K^-\pi^+)\pi^+$ decays. The uncertainty due to track reconstruction is evaluated in Belle (0.3%) using $D^{*+} \to D^0(\to K_S\,\pi^+\pi^-)\pi^+$ decays, and in Belle II (0.3%) using $e^+e^- \to \tau^+\tau^-$ events. The uncertainty due to π^0 reconstruction is estimated by comparing the ratio of efficiencies for two decay channels with different numbers of π^0's, for both data and simulation. For Belle, the ratio is the efficiency for $\eta \to \pi^0\pi^0\pi^0$ to that for $\eta \to \pi^+\pi^-\pi^0$ or $\eta \to \gamma\gamma$; the resulting uncertainty is 3%. For Belle II the ratio is the efficiency for $D^0 \to K^-\pi^+\pi^0$ to that for $D^0 \to K^-\pi^+$, and the resulting uncertainty is 5%.

Systematic uncertainties due to selection criteria are evaluated as follows. The uncertainty due to differences

TABLE II: Systematic uncertainties for the $B^+ \to \rho^+\gamma$ and $B^0 \to \rho^0\gamma$ branching fractions, isospin asymmetry, and CP asymmetry. The uncertainties on the branchng fractions are fractional, whereas the uncertainties on the asymmetries are absolute.

Source	$\mathcal{B}_{\rho^+\gamma}$ (%)	$\mathcal{B}_{\rho^0\gamma}$ (%)	$A_{\rm I}$ (%)	A_{CP} (%)
Particle detection	± 3.1	$^{+1.6}_{-1.7}$	± 1.4	$^{+0.6}_{-0.4}$
Selection criteria	$^{+7.0}_{-6.7}$	$^{+4.6}_{-4.2}$	± 4.0	$^{+0.6}_{-0.5}$
Fixed fit parameters	$^{+0.9}_{-0.8}$	$^{+3.0}_{-4.0}$	$^{+1.5}_{-2.1}$	$^{+0.3}_{-0.1}$
Signal shape	$^{+5.0}_{-2.2}$	$^{+7.2}_{-0.7}$	$^{+3.7}_{-2.5}$	$^{+0.7}_{-0.3}$
Histogram PDFs	$^{+0.0}_{-2.4}$	$^{+0.9}_{-0.3}$	$^{+1.3}_{-0.1}$	$^{+1.2}_{-0.6}$
Peaking $K^*\gamma$ bkg	± 2.6	$^{+7.3}_{-6.9}$	$^{+3.2}_{-3.1}$	$^{+0.2}_{-0.1}$
Other peaking $B\overline{B}$ bkgs	$^{+1.6}_{-1.7}$	$^{+1.0}_{-1.1}$	± 0.9	$^{+0.3}_{-0.1}$
Peaking $B\overline{B}$ A_{CP}	$^{+0.0}_{-0.2}$	$^{+0.0}_{-0.1}$	$^{+0.1}_{-0.0}$	$^{+1.0}_{-0.9}$
Number of $B\overline{B}$'s	$^{+1.3}_{-1.4}$	± 1.9	± 0.3	$^{+0.2}_{-0.1}$
$\tau_{B^\pm}/\tau_{B^0}$	$^{+0.0}_{-0.1}$	$^{+0.0}_{-0.1}$	± 0.2	< 0.1
f_{+-}/f_{00}	$^{+3.1}_{-3.0}$	± 4.7	$^{+3.8}_{-3.9}$	$^{+0.1}_{-0.0}$
Total	$^{+10.2}_{-9.3}$	$^{+12.9}_{-10.6}$	$^{+7.8}_{-7.4}$	$^{+2.0}_{-1.3}$

between data and simulation for the BDT requirements is evaluated by varying the calibration factors obtained from the $B \to \overline{D}\pi$ and $B \to K^*\gamma$ control samples by one standard deviation. The resulting uncertainties arising from the π^0 veto are 0.8% (0.7%) for the $B^+ \to \rho^+\gamma$ ($B^0 \to \rho^0\gamma$) branching fraction, and 0.7% for the isospin asymmetry. The uncertainties arising from $q\overline{q}$ suppression along with the η veto are 6.8% (4.2%) for the B^+ (B^0) branching fraction, and 3.9% for A_I. The uncertainty due to possible mis-modeling of the $B \to \overline{D}\pi^+$ control sample in Belle (see section IV A) is 0.9% (1.5%) for the B^+ (B^0) branching fraction and 0.3% for A_I. The uncertainties on A_{CP} are $O(0.1\%)$.

The uncertainty related to each fixed parameter in the fit is estimated by varying each parameter by its uncertainty and repeating the fit. The difference between the fit result and our nominal result is taken as the systematic uncertainty.

The uncertainty arising from the shape of the signal PDF is evaluated by varying the calibration factors obtained from the fit to the $B \to K^*\gamma$ control sample by their uncertainties and repeating the fit. The difference between the result and our nominal result is taken as the systematic uncertainty.

To assess the systematic uncertainty due to data-MC differences for $B \to K^*\gamma$ decays, we use the following procedure. We compare the means and widths of the $M_{\rm bc}$, ΔE, and $M(K^+\pi^{-(0)})$ distributions between data and MC for the $B \to K^*\gamma$ control sample. The shifts in means observed are negligible, but the widths have small differences. While the ratio of data-to-MC widths are almost all consistent with unity, the uncertainties on these ratios allow for differences. To estimate the effect such differences would have, we smear the simulated $B \to K^*\gamma$ events such that their $M_{\rm bc}$, ΔE, and $M(K\pi)$ distributions are broadened by the amount of the uncertainty on the data-MC ratios. We then recalculate the three-dimensional histogram PDF using these broadened distributions and refit the data for $B \to \rho\gamma$. The resulting shifts in the fit results from the nominal values are assigned as systematic uncertainties.

For the Belle II $B^0 \to K^{*0}\gamma$ control sample, the $M(K^+\pi^-)$ distribution is narrower for data than for MC, and the difference is statistically significant. Thus, for Belle II data we correct the MC $B^0 \to K^{*0}\gamma$ events such that their $M(K\pi)$ distribution is narrowed to match the data, and then re-calculate the three-dimensional histogram PDF. This PDF is used to refit the $B^0 \to \rho^0\gamma$ sample, and the shift in the fit results is assigned as a systematic uncertainty.

The systematic uncertainties due to $B\overline{B}$ background that peaks in the signal-enriched region ("peaking background") are estimated by varying this background as follows. The $K^*\gamma$ background yield is estimated as $N_{K^*\gamma} = 2 \cdot N_{B\overline{B}} \cdot \mathcal{B}(B \to K^*\gamma) \cdot F_{K/\pi} \cdot \epsilon_{K^*\gamma}$, where $F_{K/\pi}$ is the probability for a charged kaon to be misidentified as a pion, and $\epsilon_{K^*\gamma}$ is the efficiency to select $K^*\gamma$ background. The misidentification probability $F_{K/\pi}$ is obtained from a study of $D^{*+} \to D^0(\to K^-\pi^+)\pi^+$ decays; the fractional uncertainty is 6.1% for Belle and 9.7% for Belle II. To estimate the systematic uncertainty arising from $B \to K^*\gamma$ background, we vary both $\mathcal{B}(B \to K^*\gamma)$ [12] and $F_{K/\pi}$ by their uncertainties. Other peaking background sources are $B \to X_{s(d)}\gamma$ decays, where $X_{s(d)}$ is any final state of $s(d)$ quark hadronization with strangeness equal to one (zero) except for $K^*(892)\gamma$ ($\rho\gamma$), and hadronic B decays with $\pi^0(\eta) \to \gamma\gamma$ in the final states. The former is varied according to its experimental uncertainty [12]. For the latter, we take the fractional uncertainty on the number of peaking background events to be the weighted sum of the fractional uncertainties on the branching fractions for the main decay modes that contribute. For the $B^+ \to \rho^+\gamma$ mode, the contamination from $B^+ \to \rho^+\pi^0(\eta)$ decays is dominant at 24% (16%), according to the simulation. For the $B^0 \to \rho^0\gamma$ mode, the main contamination comes from $B^0 \to \rho^0\eta$ (9%), $B^+ \to a_1^+\pi^0$ (8%), and $B^+ \to \rho^+\rho^0$ (8%). For modes that have not been measured, a 50% uncertainty is assumed for the branching fractions.

For the A_{CP} measurement, we calculate the effect of a possible CP asymmetry of $B\overline{B}$ peaking background. The A_{CP} values for $B \to K^*\gamma$ and $B \to X_s\gamma$ are varied by their measured uncertainties [12], while A_{CP} for $B \to X_d\gamma$ is varied by $\pm 60\%$. The latter corresponds to a conservative uncertainty on the SM prediction [41]. The A_{CP} values for other modes such as $B \to \rho\pi^0$ are varied by $\pm 10\%$. The uncertainties on the number of $B\overline{B}$ pairs, the ratio τ_{B^+}/τ_{B^0}, and the ratio f_{+-}/f_{00} [42] are all taken into account.

VII. RESULTS

We determine the branching fractions, *CP* asymmetry, and isospin asymmetry directly from the fit. The results are

$$\mathcal{B}\left(B^+ \to \rho^+\gamma\right) = \left(13.1^{+2.0+1.3}_{-1.9-1.2}\right) \times 10^{-7} \quad (8)$$

$$\mathcal{B}\left(B^0 \to \rho^0\gamma\right) = \left(7.6 \pm 1.3^{+1.0}_{-0.8}\right) \times 10^{-7} \quad (9)$$

$$A_{CP}\left(B^+ \to \rho^+\gamma\right) = \left(-8.2 \pm 15.2^{+2.0}_{-1.3}\right)\% \quad (10)$$

$$A_{\mathrm{I}}\left(B \to \rho\gamma\right) = \left(10.9^{+11.2+6.8+3.8}_{-11.7-6.2-3.9}\right)\%, \quad (11)$$

where the first uncertainty is statistical, the second is systematic, and the third for A_{I} is the uncertainty from f_{+-}/f_{00} [42] combined with the uncertainty from the ratio of B^+ to B^0 lifetimes.

In summary, we have measured the branching fractions, direct *CP* asymmetry, and isospin asymmetry of $B \to \rho\gamma$ decays using a total of 1073 fb^{-1} of Belle and Belle II data. These results are the most precise to date and supersede the previous Belle results [7]. The results for A_{CP} and A_{I} are consistent with SM expectations.

Another parameter, as suggested in [11], is the difference from unity of the scaled ratio of isospin asymmetries:

$$\delta_{A_{\mathrm{I}}} \equiv 1 - \frac{\langle A_{\mathrm{I}}\rangle(\rho\gamma)}{\langle A_{\mathrm{I}}\rangle(K^*\gamma)} \sqrt{\frac{\bar{\Gamma}(B \to \rho\gamma)}{\bar{\Gamma}(B \to K^*\gamma)}} \left|\frac{V_{ts}}{V_{td}}\right|, \quad (12)$$

where $\bar{\Gamma}$ is the *CP*-averaged partial width. This parameter strongly depends on $\cos\phi_2$, where ϕ_2 (also known as α) is the phase $\mathrm{Arg}\left[V_{tb}^* V_{td}/\left(-V_{ub}^* V_{ud}\right)\right]$ of the CKM unitarity triangle. In the SM, $\delta_{A_{\mathrm{I}}}$ is predicted with a relatively small uncertainty: 0.10 ± 0.11. The current measured value, $\delta_{A_{\mathrm{I}}}^{\mathrm{exp}} = -4.0 \pm 3.5$, is consistent with the predicted value, albeit with a large uncertainty. Inserting our measured values for $A_{\mathrm{I}}(\rho\gamma)$ and $\mathcal{B}(B \to \rho\gamma) = \Gamma(B \to \rho\gamma) \cdot \tau_B$, along with PDG values for $A_{\mathrm{I}}(B \to K^*\gamma)$, $\mathcal{B}(B \to K^*\gamma)$, $|V_{ts}/V_{td}|$, and lifetimes τ_{B^0} and τ_{B^+} [12], we obtain

$$\delta_{A_{\mathrm{I}}} = -1.1 \pm 2.0. \quad (13)$$

This value is more precise than the previous experimental value and also consistent with the theoretical prediction.

This work, based on data collected using the Belle II detector, which was built and commissioned prior to March 2019, and data collected using the Belle detector, which was operated until June 2010, was supported by Higher Education and Science Committee of the Republic of Armenia Grant No. 23LCG-1C011; Australian Research Council and Research Grants No. DP200101792, No. DP210101900, No. DP210102831, No. DE220100462, No. LE210100098, and No. LE230100085; Austrian Federal Ministry of Education, Science and Research, Austrian Science Fund No. P 31361-N36 and No. J4625-N, and Horizon 2020 ERC Starting Grant No. 947006 "InterLeptons"; Natural Sciences and Engineering Research Council of Canada, Compute Canada and CANARIE; National Key R&D Program of China under Contract No. 2022YFA1601903, National Natural Science Foundation of China and Research Grants No. 11575017, No. 11761141009, No. 11705209, No. 11975076, No. 12135005, No. 12150004, No. 12161141008, and No. 12175041, and Shandong Provincial Natural Science Foundation Project ZR2022JQ02; the Czech Science Foundation Grant No. 22-18469S; European Research Council, Seventh Framework PIEF-GA-2013-622527, Horizon 2020 ERC-Advanced Grants No. 267104 and No. 884719, Horizon 2020 ERC-Consolidator Grant No. 819127, Horizon 2020 Marie Sklodowska-Curie Grant Agreement No. 700525 "NIOBE" and No. 101026516, and Horizon 2020 Marie Sklodowska-Curie RISE project JENNIFER2 Grant Agreement No. 822070 (European grants); L'Institut National de Physique Nucléaire et de Physique des Particules (IN2P3) du CNRS and L'Agence Nationale de la Recherche (ANR) under grant ANR-21-CE31-0009 (France); BMBF, DFG, HGF, MPG, and AvH Foundation (Germany); Department of Atomic Energy under Project Identification No. RTI 4002, Department of Science and Technology, and UPES SEED funding programs No. UPES/R&D-SEED-INFRA/17052023/01 and No. UPES/R&D-SOE/20062022/06 (India); Israel Science Foundation Grant No. 2476/17, U.S.-Israel Binational Science Foundation Grant No. 2016113, and Israel Ministry of Science Grant No. 3-16543; Istituto Nazionale di Fisica Nucleare and the Research Grants BELLE2; Japan Society for the Promotion of Science, Grant-in-Aid for Scientific Research Grants No. 16H03968, No. 16H03993, No. 16H06492, No. 16K05323, No. 17H01133, No. 17H05405, No. 18K03621, No. 18H03710, No. 18H05226, No. 19H00682, No. 20H05850, No. 20H05858, No. 22H00144, No. 22K14056, No. 22K21347, No. 23H05433, No. 26220706, and No. 26400255, and the Ministry of Education, Culture, Sports, Science, and Technology (MEXT) of Japan; National Research Foundation (NRF) of Korea Grants No. 2016R1D1A1B02012900, No. 2018R1A2B3003643, No. 2018R1A6A1A06024970, No. 2019R1I1A3A-01058933, No. 2021R1A6A1A03043957, No. 2021R1-F1A1060423, No. 2021R1F1A1064008, No. 2022R1-A2C1003993, and No. RS-2022-00197659, Radiation Science Research Institute, Foreign Large-Size Research Facility Application Supporting project, the Global Science Experimental Data Hub Center of the Korea Institute of Science and Technology Information and KREONET/GLORIAD; Universiti Malaya RU grant, Akademi Sains Malaysia, and Ministry of Education Malaysia; Frontiers of Science Program Contracts No. FOINS-296, No. CB-221329, No. CB-236394, No. CB-254409, and No. CB-180023, and SEP-CINVESTAV Research Grant No. 237 (Mexico); the Polish Ministry of Science and Higher Education and the National Science Center; the Ministry of Science and Higher Education of the Russian Federation and the HSE University Basic Research Program, Moscow; University of Tabuk Research Grants No. S-0256-1438 and No. S-0280-1439 (Saudi Arabia); Slovenian Research Agency and Research Grants No. J1-9124 and No. P1-0135; Ikerbasque, Basque Foundation for Science, the State Agency for Research of the Spanish Ministry of Science and Innovation through Grant No. PID2022-136510NB-C33, Agencia Estatal de Investigacion, Spain Grant No. RYC2020-029875-I and Generalitat Valenciana, Spain Grant No. CIDEGENT/2018/020; the Swiss National Science Foundation; National Science and Technology Council, and Ministry of Education (Taiwan); Thailand Center of Excellence in Physics; TUBITAK ULAKBIM (Turkey); National Research Foundation of Ukraine, Project No. 2020.02/0257, and Ministry of Education and Science of Ukraine; the U.S. National Science Foundation and Research Grants No. PHY-1913789 and No. PHY-2111604, and the U.S. Department of Energy and Research Awards No. DE-AC06-76RLO1830, No. DE-SC0007983, No. DE-SC0009824, No. DE-SC0009973, No. DE-SC0010007, No. DE-SC0010073, No. DE-SC0010118, No. DE-SC0010504, No. DE-SC0011784, No. DE-SC0012704, No. DE-SC0019230, No. DE-SC0021274, No. DE-SC0021616, No. DE-SC0022350, No. DE-SC0023470; and the Vietnam Academy of Science and Technology (VAST) under Grants No. NVCC.05.12/22-23 and No. DL0000.02/24-25.

These acknowledgements are not to be interpreted as an endorsement of any statement made by any of our institutes, funding agencies, governments, or their representatives.

We thank the SuperKEKB team for delivering high-luminosity collisions; the KEK cryogenics group for the efficient operation of the detector solenoid magnet; the KEK Computer Research Center for on-site computing support; the NII for SINET6 network support; and the raw-data centers hosted by BNL, DESY, GridKa, IN2P3, INFN, PNNL/EMSL, and the University of Victoria.

[1] S. L. Glashow, J. Iliopoulos and L. Maiani, Phys. Rev. D **2**, 1285-1292 (1970).
[2] A. Arhrib, C. K. Chua and W. S. Hou, Eur. Phys. J. C **21**, 567-575 (2001).
[3] A. Ali and E. Lunghi, Eur. Phys. J. C **26**, 195-200 (2002).
[4] Z. j. Xiao and C. Zhuang, Eur. Phys. J. C **33**, 349-368 (2004).
[5] X. Q. Li, Y. D. Yang and X. B. Yuan, Phys. Rev. D **89**, no.5, 054024 (2014).
[6] E. Kou *et al.* (Belle II Collaboration), PTEP **2019**, 123C01 (2019) [erratum: PTEP **2020**, 029201 (2020)], chapter 9, section 2.
[7] D. Mohapatra *et al.* (Belle Collaboration), Phys. Rev. Lett. **96**, 221601 (2006).
[8] B. Aubert *et al.* (*BABAR* Collaboration), Phys. Rev. Lett. **98**, 151802 (2007).
[9] N. Taniguchi *et al.* (Belle Collaboration), Phys. Rev. Lett. **101**, 111801 (2008).
[10] B. Aubert *et al.* (*BABAR* Collaboration), Phys. Rev. D **78**, 112001 (2008).
[11] J. Lyon and R. Zwicky, Phys. Rev. D **88**, 094004 (2013).
[12] R. L. Workman *et al.* (Particle Data Group), PTEP **2022**, 083C01 (2022).
[13] The inclusion of the charge-conjugate modes is implied throughout this paper unless otherwise stated.
[14] A. Abashian *et al.* (Belle Collaboration), Nucl. Instrum. Meth. A **479**, 117-232 (2002).
[15] J. Brodzicka *et al.*, PTEP **2012**, 04D001 (2012).
[16] S. Kurokawa and E. Kikutani, Nucl. Instrum. Meth. A **499**, 1-7 (2003).
[17] T. Abe *et al.*, PTEP **2013**, 03A001 (2013).
[18] T. Abe *et al.* (Belle II Collaboration), "Belle II Technical Design Report," arXiv:1011.0352 [physics.ins-det].
[19] D. J. Lange, Nucl. Instrum. Meth. A **462**, 152-155 (2001).
[20] R. Brun, F. Bruyant, M. Maire, A. C. McPherson and P. Zanarini, CERN-DD-EE-84-1.
[21] S. Agostinelli *et al.* (GEANT4), Nucl. Instrum. Meth. A **506**, 250-303 (2003).
[22] T. Kuhr, C. Pulvermacher, M Ritter, T. Hauth, and N. Braun, (Belle II Software Framework Group), Comput. Softw. Big Sci. **3**, 1 (2019).
[23] Belle II collaboration, Belle II Analysis Software Framework (basf2), `https://doi.org/10.5281/zenodo.5574115`.
[24] M. Gelb *et al.*, Comput. Softw. Big Sci. **2**, no.1, 9 (2018).
[25] T. Sjostrand, S. Mrenna and P. Z. Skands, JHEP **0605**, 026 (2006).
[26] R. G. Ping, Chin. Phys. C **32**, 599 (2008).
[27] T. Sjöstrand, S. Ask, J. R. Christiansen, R. Corke, N. Desai, P. Ilten, S. Mrenna, S. Prestel, C. O. Rasmussen and P. Z. Skands, Comput. Phys. Commun. **191**, 159-177 (2015).
[28] E. Barberio, B. van Eijk and Z. Wąs, Comput. Phys. Commun. **66**, 115 (1991).
[29] E. Nakano, Nucl. Instrum. Meth. A **494**, 402-408 (2002).
[30] G. C. Fox and S. Wolfram, Phys. Rev. Lett. **41**, 1581 (1978).
[31] The shower axis is defined by the line from the IP to the energy-weighted centroid of the cluster.
[32] S. Longo *et al.*, Nucl. Instrum. Meth. A **982**, 164562 (2020).
[33] E. Farhi, Phys. Rev. Lett. **39**, 1587-1588 (1977).
[34] S. H. Lee *et al.* (Belle Collaboration), Phys. Rev. Lett. **91**, 261801 (2003).
[35] H. Kakuno *et al.* (Belle Collaboration), Nucl. Instrum. Meth. A **533**, 516-531 (2004).
[36] F. Abudinén *et al.* (Belle II Collaboration), Eur. Phys. J. C **82**, 283 (2022).
[37] J. D. Bjorken and S. J. Brodsky, Phys. Rev. D **1**, 1416 (1970).
[38] M. Oreglia *et al.*, Phys. Rev. D **25**, 2259 (1982).
[39] H. Albrecht *et al.* (ARGUS Collaboration), Phys. Lett. B **241**, 278-282 (1990).
[40] H. Ikeda *et al.* (Belle Collaboration), Nucl. Instrum. Meth. A **441**, 401-426 (2000).
[41] M. Benzke, S. J. Lee, M. Neubert and G. Paz, Phys. Rev.

Lett. **106**, 141801 (2011).
[42] S. Choudhury *et al.* (Belle Collaboration), Phys. Rev. D **107**, L031102 (2023).
[43] For $a = f_{+-}/f_{00}$, $f_{+-} = a/(1+a)$ and $f_{00} = 1/(1+a)$.

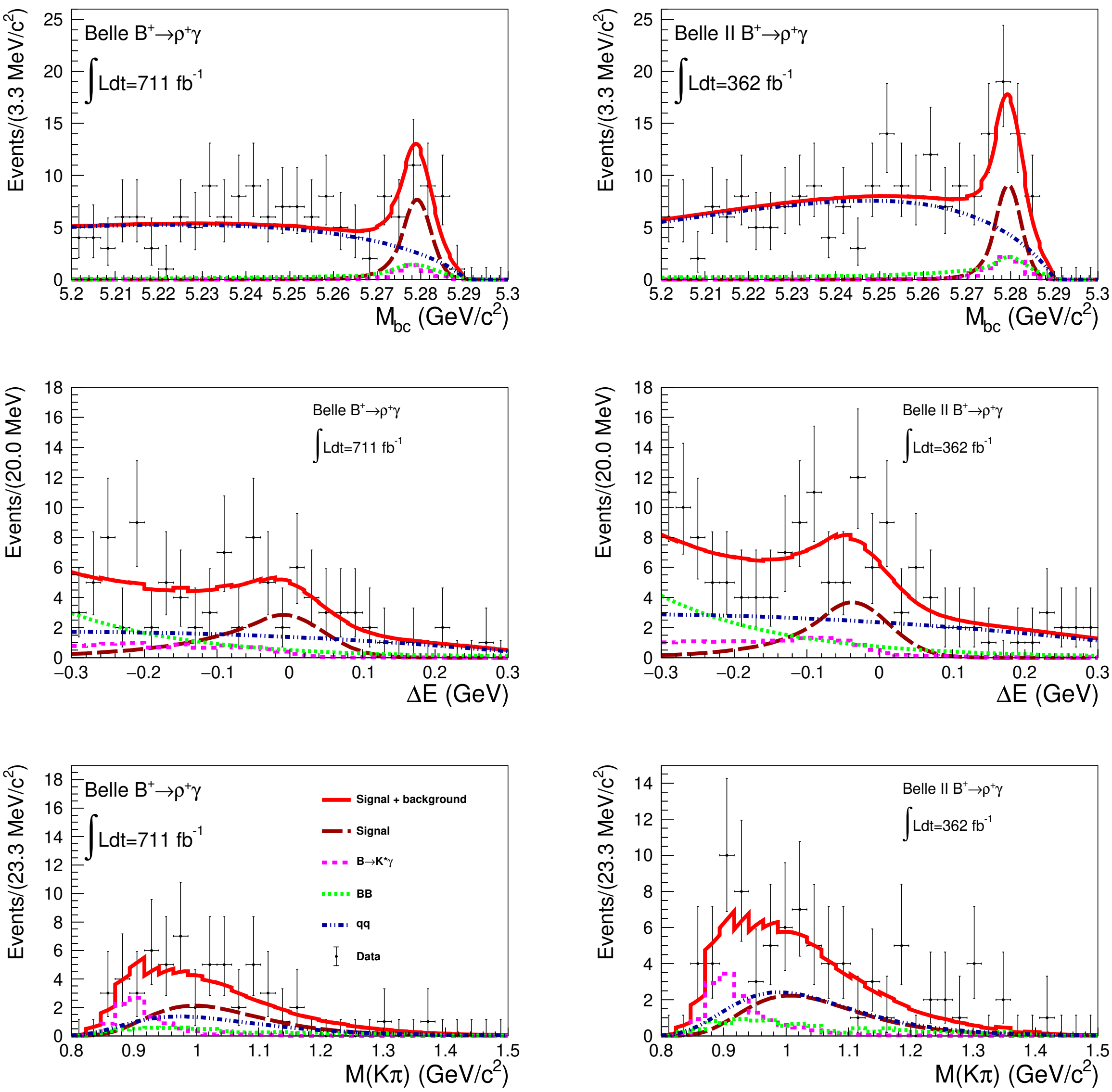

FIG. 2: Distributions of $M_{\rm bc}$, ΔE and $M(K\pi)$ for $B^+ \to \rho^+\gamma$ candidates reconstructed in the signal-enriched region of the other two variables. The signal-enriched region is defined as $M_{\rm bc} > 5.27$ GeV$/c^2$, $|\Delta E| < 0.1$ GeV and $M(K\pi) > 0.92$ GeV$/c^2$. The points with error bars are data, the solid red curves are the sum of signal and background PDFs, the dashed red curves are signal, the dotted-dashed blue curves are continuum background, the dashed magenta curves are $K^*\gamma$ background, and the dotted green curves are $B\overline{B}$ background other than $K^*\gamma$. The discrete nature of the solid red curves, which represent the signal + background fit, is due to the use of histogram PDFs for some of the backgrounds, as described in the text.

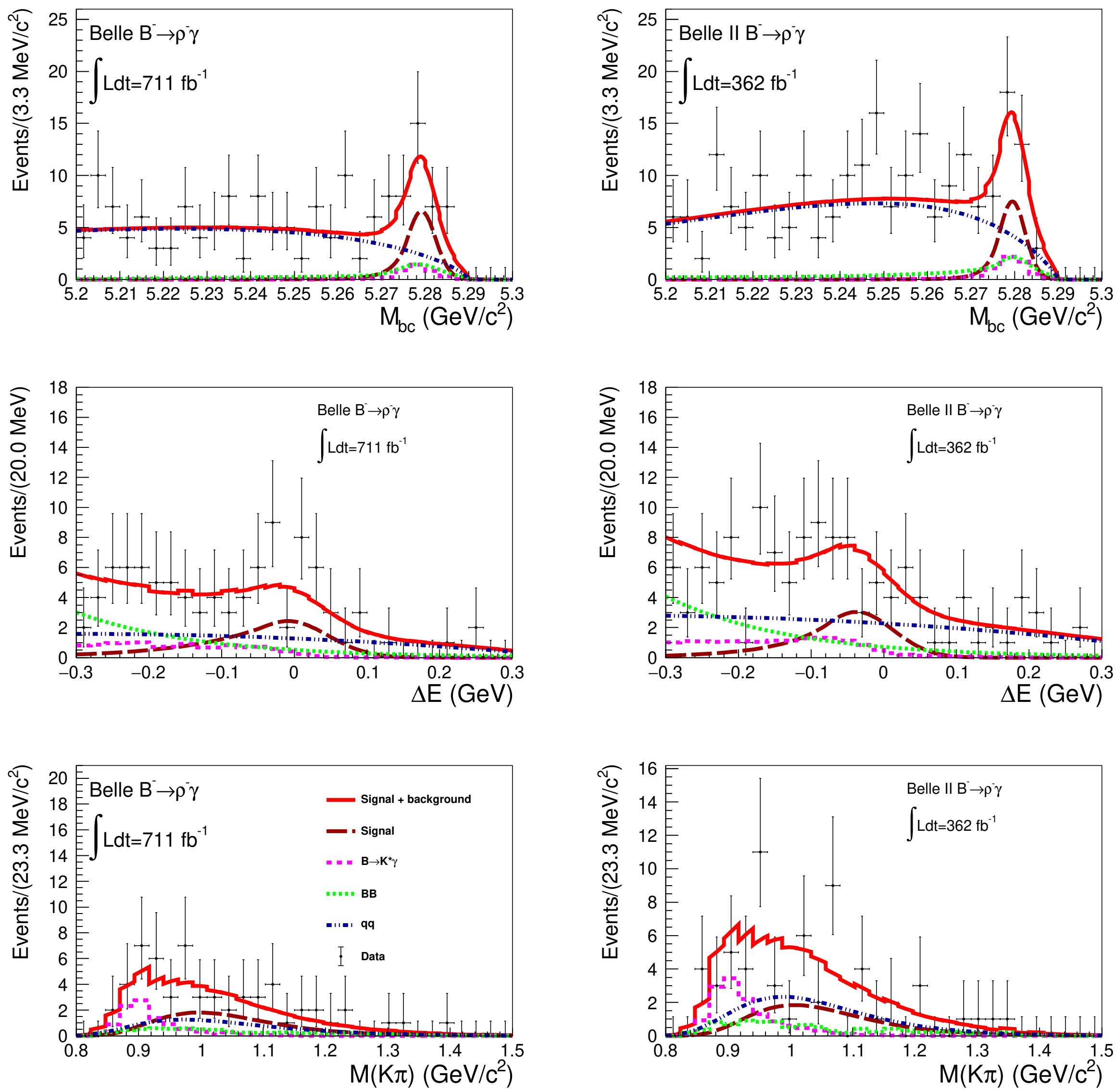

FIG. 3: Distributions of $M_{\rm bc}$, ΔE and $M(K\pi)$ for $B^- \to \rho^-\gamma$ candidates reconstructed in the signal-enriched region of the other two variables. The signal-enriched region is defined as $M_{\rm bc} > 5.27$ GeV$/c^2$, $|\Delta E| < 0.1$ GeV and $M(K\pi) > 0.92$ GeV$/c^2$. The points with error bars are data, the solid red curves are the sum of signal and background PDFs, the dashed red curves are signal, the dotted-dashed blue curves are continuum background, the dashed magenta curves are $K^*\gamma$ background, and the dotted green curves are $B\overline{B}$ background other than $K^*\gamma$. The discrete nature of the solid red curves, which represent the signal + background fit, is due to the use of histogram PDFs for some of the backgrounds, as described in the text.

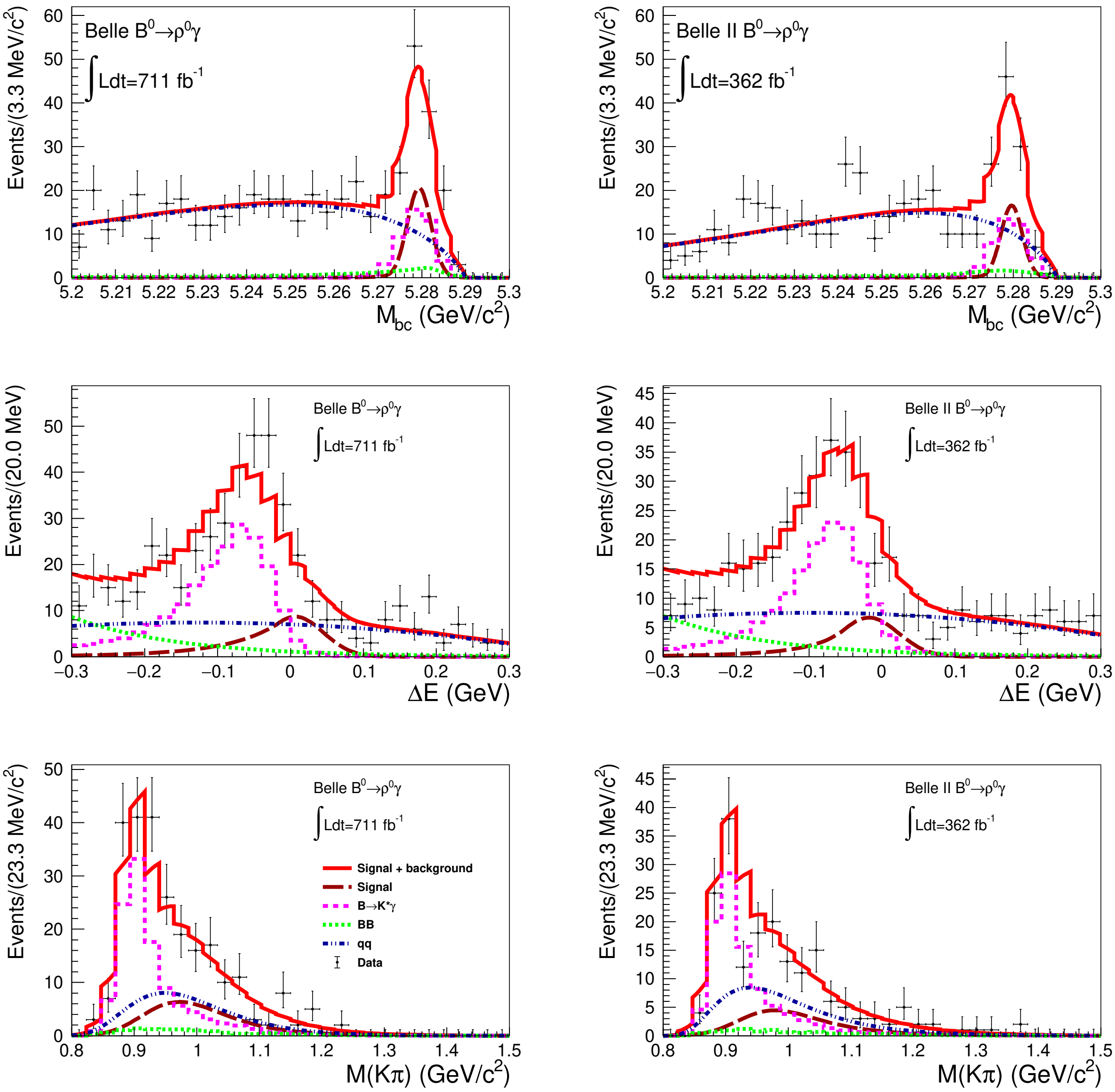

FIG. 4: Distributions of M_{bc}, ΔE and $M(K\pi)$ for $B^0 \to \rho^0\gamma$ candidates reconstructed in the signal-enriched region of the other two variables. The signal-enriched region is defined as $M_{\mathrm{bc}} > 5.27\ \mathrm{GeV}/c^2$, $|\Delta E| < 0.1$ GeV and $M(K\pi) > 0.92\ \mathrm{GeV}/c^2$. The points with error bars are data, the solid red curves are the sum of signal and background PDFs, the dashed red curves are signal, the dotted-dashed blue curves are continuum background, the dashed magenta curves are $K^*\gamma$ background, and the dotted green curves are $B\overline{B}$ background other than $K^*\gamma$. The discrete nature of the solid red curves, which represent the signal + background fit, is due to the use of histogram PDFs for some of the backgrounds, as described in the text.